Quantum Electronics **52** (6) 532–537 (2022)

https://doi.org/10.1070/QEL18071

Evolution of an ultracold gas in a non-Abelian gauge field: finite temperature effect

M. Hasan, Ch.S. Madasu, K.D. Rathod, C.C. Kwong, D. Wilkowski

Abstract. **The cooling mechanisms of a Fermionic strontium-87 gas are refined in order to study its evolution under a non-Abelian gauge field. Significant attention is paid to the effect of the finite temperature of the gas on the process in question. The efficiency of the loading of atoms in a cross-dipole trap is described in detail, the quantitative performance of the evaporative cooling is calculated, and a degenerate Fermi gas is characterised using a Thomas–Fermi distribution.**

Keywords: *ultracold Fermionic gas, cross-dipole trap, finite temperature of gas, non-Abelian gauge filed.*

1. Introduction

Gauge fields are essential ingredients of modern theories in physics [1]. A transition from the well-known Abelian gauge field U [see Eqn (1)] of quantum electrodynamics [2] to the matrix valued non-Abelian gauge field has led to the understanding of electroweak interaction [3–5], and quantum chromodynamics [6]. With the advent of quantum simulation using ultracold atomic gases, it has now been possible to mimic different model-Hamiltonians from high-energy physics, condensed matter physics, and astronomy [7–13].

One particular thing that is common to all experiments on quantum simulation of relativistic phenomena is the competition between two specific parts of the Hamiltonian, namely the kinetic energy with a quadratic dependence of momentum that has a dispersion proportional to the square-root of the temperature, and the other term arising from atom–light interaction that emulates the desired effect [14–17]. Therefore it is imperative to lower the temperature such that the kinetic energy part of the Hamiltonian becomes sub-dominant, while the term responsible for the atom–light interaction becomes dominant [16–18].

In this paper, we focus on the realisation of one specific Hamiltonian

$$\hat{H} = \frac{\hat{\boldsymbol{p}}^2}{2m} - \frac{\hat{\boldsymbol{p}}^2 \hat{\boldsymbol{A}}}{m}, \tag{1}$$

where $\hat{\boldsymbol{p}}$ is the momentum operator, m is the atomic mass, and $\hat{\boldsymbol{A}}$ is the gauge field that is a linear combination of Pauli matrices [18, 19]. In our experiment, different components of $\hat{\boldsymbol{A}}$ are non-commuting, while the underlying gauge field is non-Abelian. The second term of the Hamiltonian in Eqn (1) arises from light–matter interaction, and is proportional to the single photon recoil momentum of the atom [19]. Therefore, to observe the phenomena that arises entirely due to the second term, we need to lower the temperature so that the kinetic energy dispersion becomes sub-recoil. The aim of this present paper is to provide details on the cooling process that has led us to simulate the Hamiltonian in Eqn (1), as reported in Ref. [18]. Moreover, the behaviour of the damping motion of the dynamics as a direct consequence of the weak but finite momentum dispersion of the gas is described in detail.

2. Cooling of strontium-87 to degeneracy

The cooling of the strontium-87 atoms in our experiment consists of two major steps, namely laser cooling and evaporative cooling. The laser cooling mechanisms have already been elaborated in Refs [20–22]. Therefore, we describe thoroughly only the evaporative cooling that allows one to achieve a degenerate Fermi gas below the single photon recoil energy.

After performing laser cooling in a magneto-optical trap (MOT), about 3×10^6 atoms at a temperature of about 6 μK are loaded in a cross-dipole trap with a trap depth of $U \sim 85$ μK. The two focused beams (waist 65 μm) propagate in the horizontal plane, and cross at an angle of 70°. Their powers are controlled by acousto-optic modulators set with a 40 MHz frequency difference to average the interference effect. The wavelength of the dipole beams is 1064 nm, i.e., it is far red-detuned from the principal resonances of the strontium atom. Therefore this off-resonant dipole trap can be used to trap atoms in their ground state at high-intensity regions of the beams for a long time in a high vacuum environment (~50 s in our case) [23].

M. Hasan, Ch.S. Madasu, C.C. Kwong Nanyang Quantum Hub, School of Physical and Mathematical Sciences, Nanyang Technological University, 21 Nanyang Link, Singapore 637371 Singapore; MajuLab, International Joint Research Unit IRL 3654, CNRS, Université Côte d'Azur, Sorbonne Université, National University of Singapore, Nanyang Technological University, Singapore;
K.D. Rathod Centre for Quantum Technologies, National University of Singapore, 117543 Singapore; MajuLab, International Joint Research Unit IRL 3654, CNRS, Université Côte d'Azur, Sorbonne Université, National University of Singapore, Nanyang Technological University, Singapore;
D. Wilkowski Nanyang Quantum Hub, School of Physical and Mathematical Sciences, Nanyang Technological University, 21 Nanyang Link, Singapore 637371 Singapore; MajuLab, International Joint Research Unit IRL 3654, CNRS, Université Côte d'Azur, Sorbonne Université, National University of Singapore, Nanyang Technological University, Singapore; Centre for Quantum Technologies, National University of Singapore, 117543 Singapore; e-mail: david.wilkowski@ntu.edu.sg

Received 14 March 2022
Kvantovaya Elektronika **52** (6) 532–537 (2022)
Submitted in English

After loading the dipole trap, the beam powers are maintained maximal for 3 s for the atoms at the wings of the each Gaussian beams to leave the trap. To characterise the loading efficiency, we quantify the number of loaded atoms and the equilibrium temperature for different values of trap depths, as shown in Fig. 1. One can see that the number of atoms increases linearly along with a linear increase in temperature, and when the trap depth U increases by 1 μK, we load about $\sim 4.3 \times 10^4$ more atoms into the dipole trap at the expense of an increased temperature by 100 nK. The number of atoms in the last stage of laser cooling is about 15×10^6. Therefore at a maximum trap depth, around 15% of the atoms are transferred into the dipole trap.

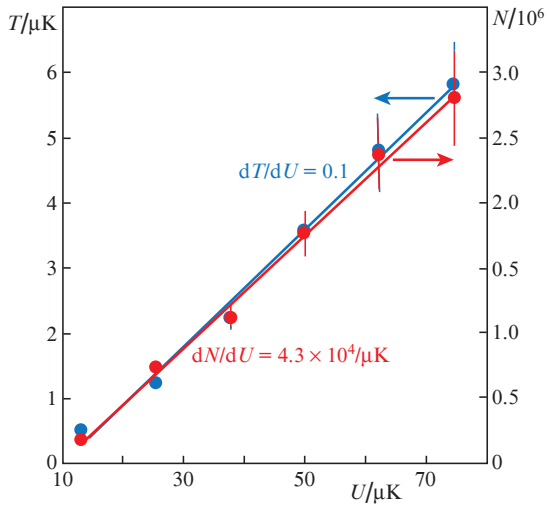

Figure 1. (Colour online) Number of atoms loaded into the dipole trap (red dots) and the temperature of the gas (blue dots) as a function of the maximum trap depth U. The solid lines are linear fits. The mentioned trap depth is determined for the ground state $^1S_0$ and is estimated theoretically from the measured power of the beams [23].

After thermalisation, we perform optical pumping to transfer all the atoms with positive m_F values of the $F_g = 9/2$ ground states to the $|F_g = 9/2, m_F = 9/2\rangle$ state, while the atoms with negative m_F values remain intact providing thermalisation during the evaporative cooling.

Our scheme for evaporative cooling is composed of three stages (Fig. 2a). Stage 1 is the idle evaporation lasting for 3 s. After that the power of both beams starts decreasing according to the dependences shown by blue and red curves. This is stage 2 of the evaporative cooling, which lasts for 2.22 s, till the power of one of the beams reaches a value that is slightly above the power necessary to hold the entire cloud against gravity (dashed black line $P_{gravity}$). At stage 3, the power of one of the beams is held fixed, while the power of the other beam continues to lower, which leads to a decrease in the trap depth. Stage 3 terminates in 5.5 s. At stage 3, the power of only one beam is decreases and, therefore, we call this stage 2D evaporation, in contrast to 3D evaporation at stage 2 where the trap depth is lowered in the three spatial directions.

To quantify the full trajectory of evaporation, we measure the number of atoms N and the corresponding temperature T at different moments of time during evaporation, as shown in Fig. 2b. One can see that the temperature continues to drop, accompanied by atom losses due to evaporation.

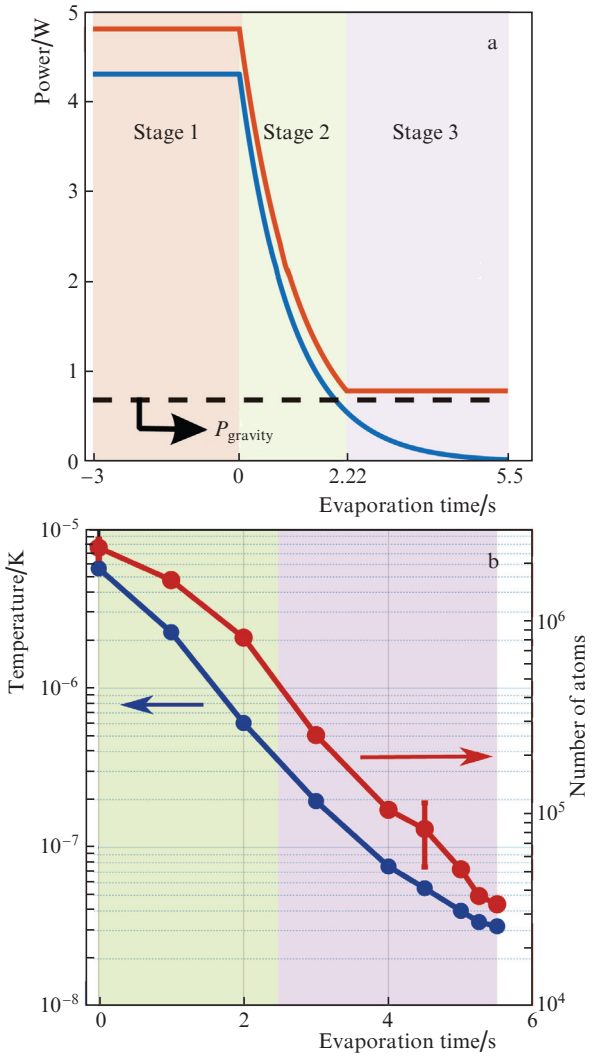

Figure 2. (Colour online) Dependences of (a) the powers of two focused beams composing a dipole trap, as well as of (b) the temperature (blue dots) and the number of atoms (red dots) on the evaporation time.

To quantify the efficiency of the evaporation, we consider two particular metrics:

1. The quantity $\partial \mathrm{Log}\, N / \partial \mathrm{Log}\, T$ is the slope that estimates the efficiency of evaporation. When this quantity is smaller than the dimensionality D of evaporation, it implies efficient evaporation, namely a net increase in the phase-space density [24].

2. The quantity T/T_F where T_F is the Fermi temperature of the gas; a smaller value below unity implies a gas approaching a degenerate state.

Figure 3a shows that during stage 2, evaporation is extremely efficient as the slope 0.48 in the log–log scale is much smaller than the dimensionality $D = 3$. However, the efficiency drops during stage 3. Nevertheless, the slope 1.1 is still larger than the dimensionality $D = 2$. A decrease in efficiency during the later stage of evaporation is expected for a fermionic species since the Pauli exclusion principle inhibits the collisions among the atoms with same internal state, when the gas enters into the degenerate regime. The Pauli blockade is also manifested in the right panel of Fig. 3b near the end of stage 3, via the flattening of T/T_F.

At the end of evaporation, we are left with a gas of 3.7×10^4 atoms in the $|F_g = 9/2, m_F = 9/2\rangle$ state at a temperature of

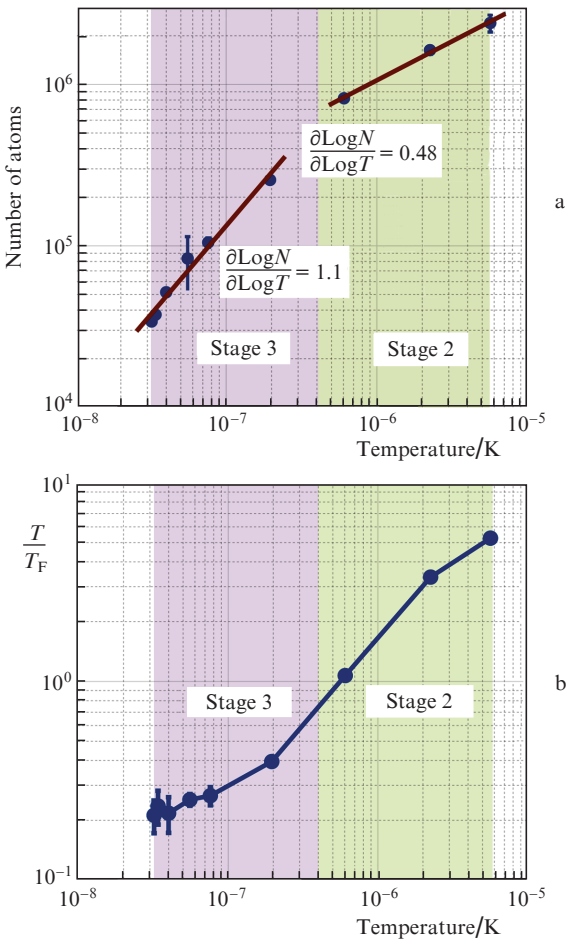

Figure 3. (Colour online) Temperature dependences of (a) the number and (b) degeneracy parameter in the course of evaporation. The solid red curves are linear fits of the experimental data.

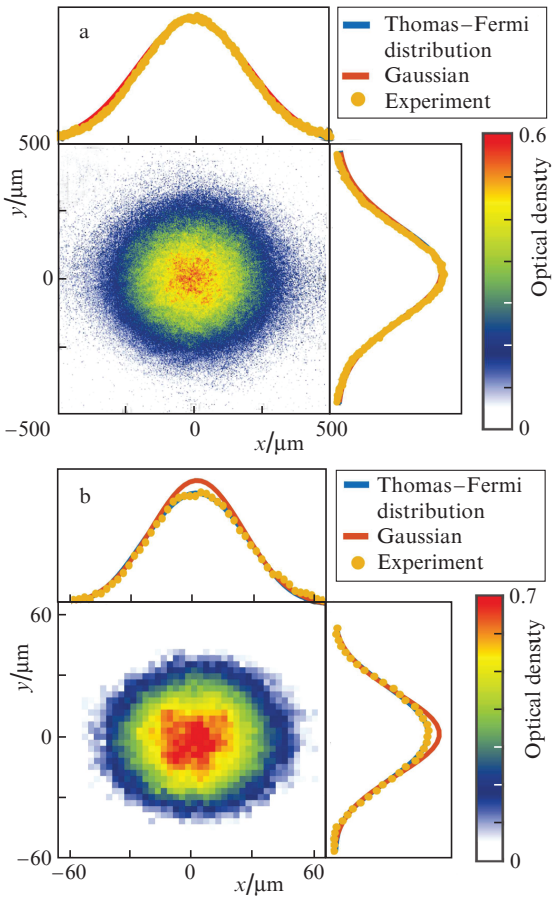

Figure 4. (Colour online) Spatial distributions of atoms in the thermal equilibrium at T/T_F = (a) 3.1 and (b) 0.21 after 13 ms of time-of-flight.

~30 nK with $T/T_F = 0.21$. In order to extract the relevant thermodynamic quantities of the gas, we fit the momentum distribution of the gas with Thomas–Fermi distribution (see [16] for detail). Figure 4a shows a nondegenerate gas at $T/T_F = 3.1$, in which the momentum distribution of the gas is well described by the Gaussian function capturing a classical Maxwell–Boltzmann distribution. Note that at large T/T_F the Thomas–Fermi distribution reduces to a Maxwell–Boltzmann momentum distribution [16, 25]. In contrast, a degenerate Fermi gas deviates from the Maxwell–Boltzmann distribution, as shown in Fig. 4b at $T/T_F = 0.21$. An essential feature of the degeneracy is the overshoot of the Maxwell–Boltzmann momentum distribution, seen via the integrated optical density along each axis in Fig. 4b.

After evaporation, the atoms are either in the $|F_g = 9/2, m_F = 9/2\rangle$ state or in the $|F_g = 9/2, m_F < 0\rangle$ state. The atoms with $m_F < 0$ are necessary to thermalise the atoms with $m_F = 9/2$ during evaporation, but remain spectators in our experiment with the gauge field. In preparing a cold gas with a temperature of 40–50 nK, we turn on the appropriate laser beams to create an artificial non-Abelian gauge field for atoms with $m_F = 9/2$ only and observe the evolution of the ultracold gas in the gauge field, as described in the following section.

3. Evolution in a two-dimension non-Abelian gauge field

We realise a 2D non-Abelian gauge field, where the governing Hamiltonian is given by Eqn (1). With the explicit form of the realised gauge field $\hat{\boldsymbol{A}}$, the matrix Hamiltonian has the form

$$\hat{H} = \frac{\hat{\boldsymbol{p}}^2}{2m} + \frac{\hbar k}{2\sqrt{3}\,m}\begin{bmatrix} -\sqrt{3}\,(3\hat{p}_x + \hat{p}_y) & (\hat{p}_y - \hat{p}_x) \\ (\hat{p}_y - \hat{p}_x) & (1/\sqrt{3})(3p_x + \hat{p}_y) \end{bmatrix}, \quad (2)$$

where $\hat{p}_{x,y}$ are the two components of the momentum operator, and k is the wave number of the laser beams that produce the artificial gauge field. The Hamiltonian is expressed in the so-called dark-state basis of a tripod scheme [18, 19, 26]. The latter consists of three ground states $|F_g = 9/2, m_F = 5/2\rangle \equiv |5/2\rangle_g$, and $|F_g = 9/2, m_F = 7/2\rangle \equiv |7/2\rangle_g$, $|F_g = 9/2, m_F = 9/2\rangle \equiv |9/2\rangle_g$, optically coupled to a unique excited state $|F_e = 9/2, m_F = 7/2\rangle \equiv |7/2\rangle_e$, as depicted in Fig. 5. The two dark states, extracted from the dressed state picture, are degenerated and read,

$$|D_1\rangle = \frac{\exp(-2ikx)\,|5/2\rangle_g - \exp[-ik(x+y)]\,|7/2\rangle_g}{\sqrt{2}}, \quad (3)$$

$$|D_2\rangle = \frac{\exp(-2ikx)\,|5/2\rangle_g + \exp[-ik(x+y)]\,|7/2\rangle_g - 2\,|9/2\rangle_g}{\sqrt{6}}, \quad (4)$$

if the Rabi frequencies of the tripod beams are the same (210 kHz in our experiment). Note that these states do not contain the excited state and are thus immune to decoherence by spontaneous emission processes. On the contrary, two other states that complete the basis are called bright states because they contain the excited state. Fortunately, they can be energetically decoupled to the dark states (adiabatic approximation). We performed our experiment under this regime, namely in the dark state manifold as discussed in Refs [18, 27].

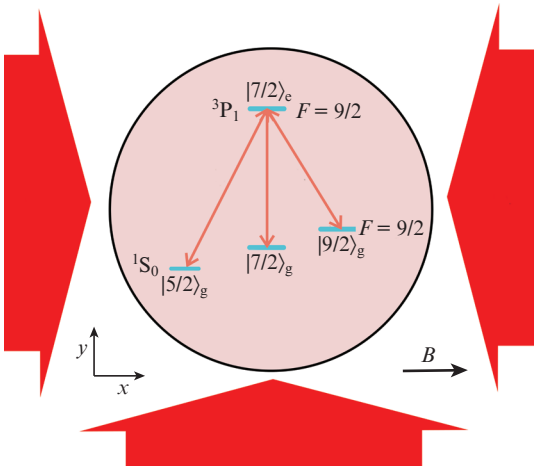

Figure 5. (Colour online) Excitation of an atom according to the scheme of the internal tripod, which is resonantly coupled with two counter-propagating laser beams along the x axis with polarisations σ_+ and σ_-, and a third beam with π polarisation along the y axis (red arrows). A magnetic field $B = 67$ G along the axis makes it posible to isolate the tripod within the $F_g = 9/2 \rightarrow F_e = 9/2$ hyperfine transition of the intercombination line.

To transfer the atoms from the $|9/2\rangle_g$ state to the dark state, we turn on the two beams with polarisations σ_+ and π shown in Fig. 5. After 1 μs, the beam with the polarisation – that acts on the atoms in the $|9/2\rangle_g$ state is turned on. This scheme makes it possible to populate the dark state $|D_2\rangle$ described by Eqn (4).

After preparing the ultracold gas in the dark-state $|D_2\rangle$, we observed its dynamics at different mean momenta $\boldsymbol{P}$ with a magnitude P_0 at an angle Θ with respect to the x axis, shown in Fig. 6. Using fluorescence imaging, we measured the population P_{m_F} in the ground states m_F. Afterwards, we converted the populations to the velocities along x and y axes using the relations [18]:

$$v_x = -v_r(2P_{5/2} + P_{7/2}),$$
$$v_y = -v_x(P_{7/2}), \tag{5}$$

where $v_r = \hbar k/m$ is the single photon recoil velocity.

As shown in Fig. 6, the velocity oscillation depends strongly on the mean momentum of the atoms along with the angle Θ. The amplitudes of the velocity components as function of Θ are shown in Fig. 7 for a fixed value of P_0. One can see that the velocity amplitudes along each axis vary strongly as a function of Θ for a fixed value of $P_0 = 4\sqrt{2}$ given in the recoil momentum units. The expression of the velocity components at finite temperature T has the form [18]

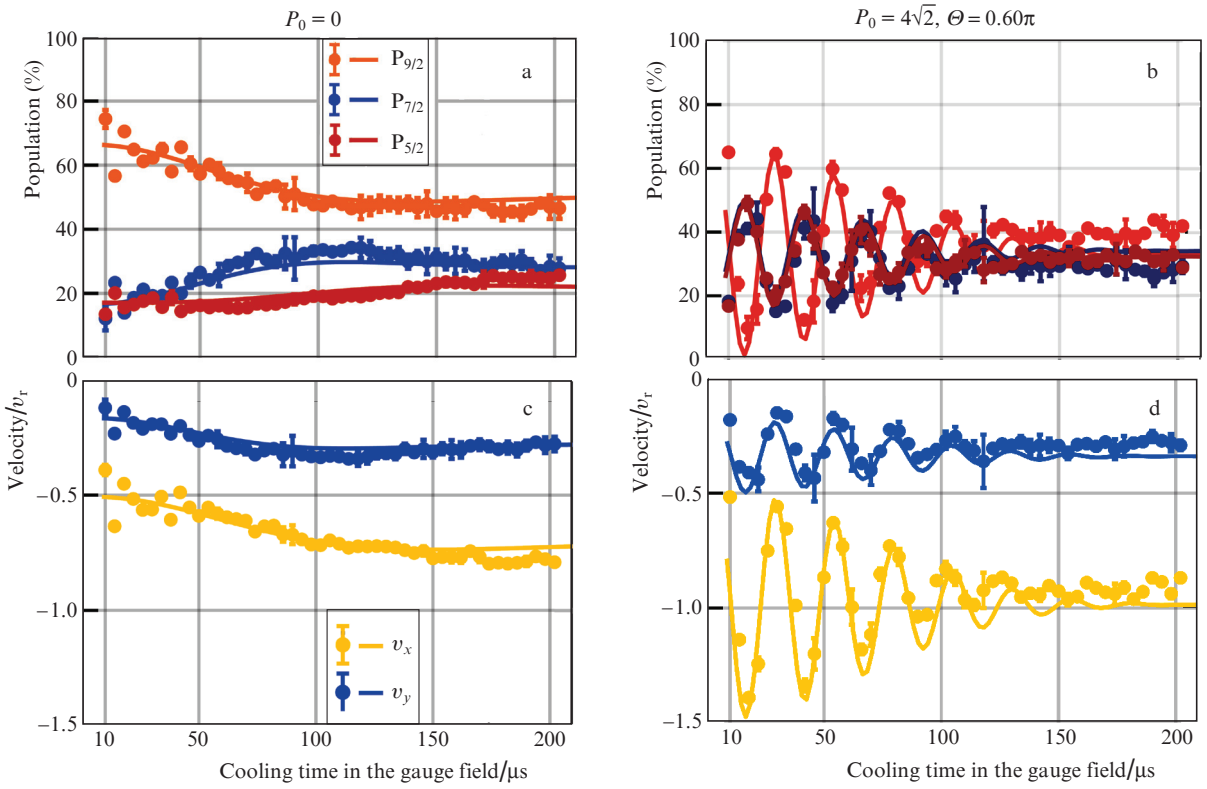

Figure 6. (Colour online) Time dependences of the population and recoil velocity projection at different values of the magnitude of momenta and angles for (a, b) the population P_{m_F} of the three atomic ground states and (c, d) the velocity components. The dots are the values extracted from experiments, and the solid curves are the numerical calculation using Heisenberg equation of motion without free fitting parameters [18].

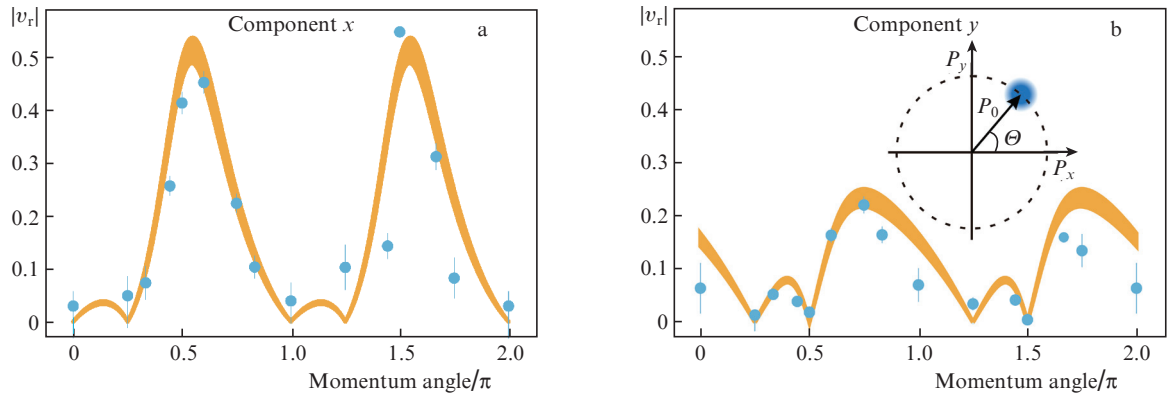

Figure 7. (Colour online) Dependences of the amplitudes of (a) x and (b) y components of the velocity. The inset in panel (b) shows a nonzero momentum of the atomic wavepacket (schematically shown as a blue disk), with magnitude $P_0 = 4\sqrt{2}$ at an angle Θ to the x axis. The solid strips are theory prediction given by Eqn (7) while accounting for finite ramping time of the tripod laser.

$$
\begin{aligned}
v_x(P_0,\Theta;t) &\approx v_{x1} + v_{x0}\cos(\omega t)\exp[-(t/\tau)^2],\\
v_y(P_0,\Theta;t) &\approx v_{y1} + v_{y0}\cos(\omega t)\exp[-(t/\tau)^2],\\
\omega &= \frac{2k}{3m}P_0\sqrt{2+\cos(2\Theta)},\\
\tau &= \frac{3}{k}\sqrt{\frac{m}{2k_{\mathrm{B}}T}}\sqrt{\frac{2+\cos(2\Theta)}{5+4\cos(2\Theta)}},
\end{aligned}
\tag{6}
$$

where the momentum distribution of the gas is approximated by a Maxwell–Boltzmann distribution. The offset and the amplitude of each velocity component are expressed as:

$$
\begin{aligned}
v_{x1} &= \frac{\hbar k}{m}\frac{\sin(2\Theta)-\cos(2\Theta)-5}{4[2+\cos(2\Theta)]},\\
v_{x0} &= \frac{\hbar k}{m}\frac{1}{\sqrt{2}}\frac{\sin\Theta\sin(\Theta-\pi/4)}{2+\cos(2\Theta)};
\end{aligned}
\tag{7}
$$

$$
\begin{aligned}
v_{y1} &= \frac{\hbar k}{m}\frac{3\sin(2\Theta)-5\cos(2\Theta)-7}{12[2+\cos(2\Theta)]},\\
v_{y0} &= \frac{\hbar k}{m}\frac{1}{\sqrt{2}}\frac{\cos\Theta\sin(\pi/4-\Theta)}{2+\cos(2\Theta)}.
\end{aligned}
$$

The frequency of the velocity oscillation ω in Eqn (6) depends both on the magnitude and the slope of the vector $\boldsymbol{P}$, while the velocity amplitudes (7) depend only on the angle Θ. This dependence leads to the anisotropic behaviour observed in the experiment. Note that both velocity components vanish at $\Theta = \pi/4$ and $5\pi/4$. At these angles, the dark state $|D_2\rangle$, which is the initial state for all the experiments, is an eigenstate of the Hamiltonian, and leads to the suppression of the oscillation [18].

The anisotropy of the damping time τ of the velocity oscillation is shown in Fig. 8. One can see that the damping time τ (orange circles) depends on the direction of the mean momentum imparted to the atoms. The solid blue curve is the theory prediction of τ from Eqn (5), where we have used a Maxwell–Boltzmann velocity distribution. Note that although the theory captures the trend of the experimental data, the estimation from theory generally overestimates the damping time measured in the experiment. We also performed a simulation of the dynamic of the gas using the Hamiltonian

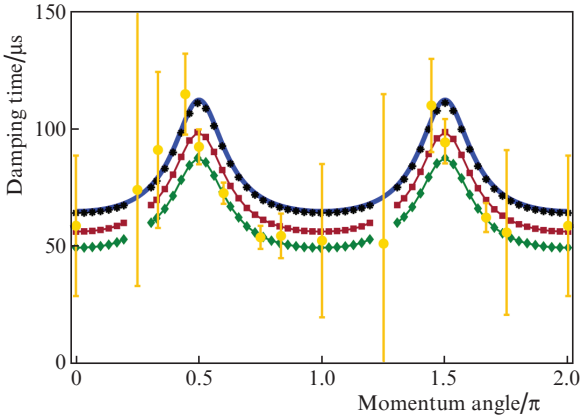

Figure 8. Damping time τ of the velocity vs. momentum angle Θ (the orange circles are the result of the fitting with a damped oscillation of the experimental data; the blue curve is the theory prediction from Eqn (5); the black stars, red squares, and green diamonds correspond to a simulation with a Maxwell–Boltzmann distribution, a Fermi–Dirac distribution with $T/T_{\mathrm{F}} = 0.3$, and a Fermi–Dirac distribution with $T/T_{\mathrm{F}} = 0.2$, respectively). The fitting procedure is disregarded in the vicinity of $\Theta = \pi/4$ and $\Theta = 5\pi/4$, where oscillations vanish.

(see Eqn 1) in the Heisenberg approach. We then fitted the damping of the oscillation using an exponential decay. With a Maxwell–Boltzmann distribution (black stars), the fitted decay time is in perfect agreement with the theory prediction from Eqn (5).

We also take into account the role of the Fermi statistic, with decays obtained for $T/T_{\mathrm{F}} = 0.3$ ($T/T_{\mathrm{F}} = 0.2$) corresponding to the red squares (green diamonds). The reduction of the damping time with a Fermi–Dirac distribution can be simply understood by a reduction of the low momentum population with respect to the Maxwell–Boltzmann distribution.

.

4. Conclusions

We have studied the loading of atoms in a cross-dipole trap and their evaporative cooling to reach a degenerate state at $T/T_{\mathrm{F}} = 0.21$. The evaporative cooling of the atoms with proper characterisation of the efficiency is described in detail. This cold gas is used further to observe the anisotropic zitterbewegung dynamics of the ultracold in a 2D non-Abelian

gauge field. The role of Fermi degeneracy is emphasised to understand extra damping of the velocity dynamics.

Acknowledgements. This work was supported by the CQT/MoE funding (Grant No. R-710-002-016-271), and the Singapore Ministry of Education Academic Research Fund (Tier1 Grant No. MOE2018-T1-001-027 and Tier2 Grant No. MOE-T2EP50220-0008).

References

1. Cheng T.-P., Li L.-F. *Gauge Theory of Elementary Particle Physics* (Oxford University Press, 1994).
2. Peskin M.E. *An Introduction to Quantum Field Theory* (CRC Press, 2018).
3. Salam A., Ward J.C. *Il Nuovo Cimento*, **11**, 568 (1959).
4. Weinberg S. *Phys. Rev. Lett*., **19**, 1264 (1967).
5. Glashow S.L. *Nucl. Phys*., **10**, 107 (1959).
6. Marciano W., Pagels H. *Phys. Rep*., **36**, 137 (1978).
7. Görg F., Sandholzer K., Minguzzi J., Desbuquois R., Messer M., Esslinger T. *Nat. Phys*., **15**, 1161 (2019).
8. Barberán N., Dagnino D., GarcíaMarch M.A., Trombettoni A., Taron J., Lewenstein M. *New J. Phys*., **17**, 125009 (2015).
9. Homeier L., Schweizer C., Aidelsburger M., Fedorov A., Grusdt F. ArXiv:2012.05235.
10. Schweizer C., Grusdt F., Berngruber M., Barbiero L., Demler E., Goldman N., Bloch I., Aidelsburger M. *Nat. Phys*., **15**, 1168 (2019).
11. Barbiero L., Schweizer C., Aidelsburger M., Demler E., Goldman N., Grusdt F. *Sci. Adv*., **5**, eaav7444 (2019).
12. Banik S., Gutierrez Galan M., Sosa-Martinez H., Anderson M., Eckel S., Spielman I.B., Campbell G.K. *Phys. Rev. Lett*., **128**, 090401 (2022).
13. Eckel S., Kumar A., Jacobson T., Spielman I.B., Campbell G.K. *Phys. Rev.*, **X 8**, 021021 (2018).
14. Lin Y.-J., Compton R.L., Jiménez-García K., Porto J.V., Spielman I.B. *Nature*, **462**, 628 (2009).
15. LeBlanc L.J., Beeler M.C., Jiménez-García K., Perry A.R., Sugawa S., Williams R.A., Spielman I.B. *New J. Phys*., **15**, 073011 (2013).
16. Hasan M. PhD Thesis (Nanyang Tecnological University, 2021).
17. Sugawa S., Salces-Carcoba F., Yue Y., Putra A., Spielman I.B. ArXiv:1910.13991.
18. Hasan M., Madasu C.S., Rathod K.D., Kwong C.C., Miniatura C., Chevy F., Wilkowski D. ArXiv:2201.00885.
19. Dalibard J. Gerbier F., Unas G.J., Öhberg P. *Rev. Mod. Phys*., **83**, 1523 (2011).
20. Chaneliere T., He L., Kaiser R., Wilkowski D. *Europ. Phys. J. D*, **46**, 507 (2008).
21. Chalony M., Kastberg A., Klappauf B., Wilkowski D. *Phys. Rev. Lett*., **107**, 243002 (2011).
22. Yang T., Pandey K., Pramod M.S., Leroux F., Kwong C.C., Hajiyev E., Chia Z.Y., Fang B., Wilkowski D. *Europ. Phys. J. D*, **69,** 226 (2015). DOI: 10.1140/epjd/e2015- 60288-y.
23. Grimm R., Weidemüller M., Ovchinnikov Y.B. *Optical Dipole Traps for Neutral Atoms* (Academic Press, 2000) pp 95–170.
24. Valtolina G., Matsuda K., Tobias W.G., Li J.-R., De Marco L., Ye J. ArXiv:2007.12277.
25. Sanner C., Su E.J., Keshet A., Gommers R., Shin Y.-Il., Huang W., Ketterle W. *Phys. Rev. Lett*., **105**, 040402 (2010).
26. Ruseckas J., Juzeliūnas G., Öhberg P., Fleischhauer M. *Phys. Rev. Lett*., **95**, 010404 (2005).
27. Leroux F., Pandey K., Rehbi R., Chevy F., Miniatura C., Grémaud B., Wilkowski D. *Nat. Commun*., **9**, 3580 (2018).